Lasers, lenses and light curves : adaptive optics microscopy and peculiar transiting exoplanets

Werkhoven, T.I.M.

CHAPTER 6

Analysis of *SuperWASP* J140747.93−394542.6 transit fine-structure: hints of exomoons

T. I. M. van Werkhoven, M. A. Kenworthy and E. E. Mamajek *Monthly Notices of the Royal Astronomical Society* (accepted)

A recently discovered $V = 12.3$ mag K5 star in the *SuperWASP* database shows a peculiar light curve with a highly structured eclipse pattern covering a timespan of at least 54 d with maximum dimming of at least 3.3 mag (Mamajek et al., 2012). The central eclipse is surrounded by two 1 mag eclipses at ± 12 d and ± 26 d. The authors speculate that the star is eclipsed by a substellar companion with an extended and highly structured ring system. To investigate the nightly light curve structure and to confirm the multiple ring hypothesis, we have carried out a calibrated reduction of the *SuperWASP* data, removing both systematic errors and periodic stellar variability. We count at least 24 inflection points on ingress and 16 on egress, consistent with the presence of at least 24 rings in this disk. By measuring the light curve gradient, we find implied speeds for the eclipsing object that are incompatible with a closed Kepler orbit with $P = 2.3$ yr. We propose several scenarios that could give rise to such light curve gradients and find that azimuthal ring structure (analogous to "spokes" seen in

Saturn's rings) can account for the observed light curve. The highly structured ring system also implies the presence of exomoons orbiting the secondary companion.

6.1 Introduction

Mamajek et al. (2012) discovered the peculiar light curve of a young ~16 Myr, 0.9 $M_\odot$, $V = 12.3$ mag K5 star (1SWASP J140747.93−394542.6 = ASAS J140748−3945.7, hereafter J1407) in *The Super Wide Angle Search for Planets* (henceforth *SuperWASP*) database. The light curve as observed by *SuperWASP* shows a deep >3.3 mag eclipse with two pairs of eclipses occurring symmetrically 12 d and 26 d before and after the eclipse midpoint, parts of which are confirmed by the lower-cadence *All Sky Automated Survey* data. Light curve variability induced by extended disk eclipses is not unique, as seen in the stars EE Cep (Mikolajewski & Graczyk, 1999) and ϵ Aurigae (Guinan & Dewarf, 2002) which show related complex asymmetric eclipses caused by discs orbiting the primary star.

The authors propose and reject several explanations for these observations. An eclipse by an isolated (sub)stellar companion alone would not yield a >95 per cent dimming, nor does it explain the eclipse fine-structure seen in the nightly photometry. An eclipsing binary where a red giant eclipses a fainter, bluer star is rejected on spectroscopic grounds; there is no evidence for a giant in J1407, nor would it give rise to the structure observed in the eclipse weeks before and after the primary eclipse. A disk orbiting an old stellar remnant companion obscuring the primary is unlikely because the system is very young. A circumbinary or circumstellar disk obscuring the primary is unlikely because there is no excess infrared observed at J1407 indicative of such a thick disk. Additionally, the period is incompatible with this scenario. A disk orbiting J1407 obscuring the star light due to the relative motion between us and J1407 would yield a one-time eclipsing event, but is disregarded because it requires a very thin disk (aspect ratio height over radius $\sim 10^{-8}$) and it does not explain the symmetric dimming around the central minimum. Finally, a more massive companion obscured by a disc orbiting it is unlikely again due to lack of infrared excess.

The scenario Mamajek et al. (2012) propose involves a circumsecondary or circumplanetary disc (similar to ϵ Aurigae; Guinan & Dewarf, 2002), which obscures the primary star, J1407. Based on the absence of a second transit, the authors constrain the period $P > 2.33$ yr, yielding an orbital radius greater than 1.7 AU and a circular orbital velocity less than 21.7 km s^{-1} (assuming $m_1 = 0.9\,M_\odot$). They propose a preliminary 4-ring model with

a central opaque disk accompanied by three discrete rings with opacities $\tau = 0.5, 0.2, 0.05$. To match the observations, this model has an orbital inclination of 89.955° and the ring plane is tilted by 13° to the orbital plane.

In this paper, we carry out a new reduction of the *SuperWASP* data, taking care of systematic inter-CCD differences and additionally remove stellar variability due to the rotation of the star (described in Sect. 6.2). We then investigate the nightly fine structure in the photometric signal, focusing specifically on the light curve gradient and its implications for the nature of the eclipsing structure (Sect. 6.4 and Sect. 6.5). We construct a toy-model for the ring system consisting of N discrete rings with variable opacity which we fit to the cleaned up photometric signal in Sect. 6.6. We propose several possible scenarios for these findings and conclude with suggestions to better constrain the system in Sect. 6.7.

6.2 Data reduction

The Super Wide Angle Search for Planets (*SuperWASP*; Pollacco et al., 2006) observatories are located at the Observatorio del Roque de los Muchachos on La Palma, and at the Sutherland Station of the South African Astronomical Observatory. Both facilities consist of a telescope with eight lenses (Canon 200 mm $f/1.8$), each mounted on a 2048×2048-pixel back-illuminated CCD (e2v). Each lens has a field of view of ~64 deg^2, for a total of ~482 deg^2 per telescope. The data acquisition cadence is 9 to 12 min for each camera (Butters et al., 2010).

The *SuperWASP* database has coverage of J1407 during the seasons of 2006 through 2008 (depicted in the upper panel of Fig. 6.1). The star was observed on CCDs 221, 227, and 228. CCDs 227 and 228 have coverage of J1407 during 2006, 2007 and 2008, while CCD 221 only has coverage during the 2007 season. The *SuperWASP* pipeline provides simple aperture photometry (Kane et al., 2004), as well as automatically reduced flux according to the `TAMUZ` correction (Cameron et al., 2007; Tamuz et al., 2005). We find that the automatic correction does not produce optimal photometry for this specific target, which can be expected considering the peculiar behaviour of the light curve (see Fig. 6.3) and the star's location at the corner of the field of view of the three cameras.

Because of this variability, we began our reduction with the simple aperture photometry flux instead of using the automatically reduced flux. First we de-correlated the systematic errors from the light curve by using a selected ensemble of nearby stars to act as a photometric standard, allowing direct comparison of the data from different CCDs (Sect. 6.2). After de-

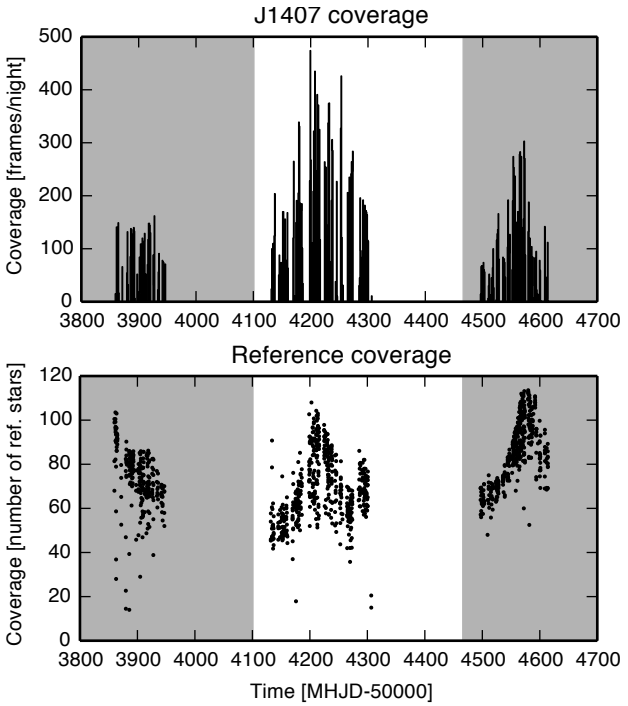

Figure 6.1: *Top:* Number of *SuperWASP* observations of J1407, summed for all CCDs. *Bottom:* Number of reference stars co-temporally observed with J1407 for all CCDs, averaged per day. Years 2006 and 2008 are shaded. The transit occurred in 2007 around MHJD 54 222.

correlation, we removed the stellar variability from the light curve through phase dispersion minimisation (Sect. 6.2).

Systematics de-correlation

The multiple CCDs of *SuperWASP* provide significantly different light curves, as observed by Mamajek et al. (2012) and Norton et al. (2011). To mitigate this effect, we de-correlated systematic errors between the CCDs based on Tamuz et al. (2005) and de-correlation techniques used by *Kepler* (Fraquelli & Thompson, 2012, p. 21)[1].

First we select a set of 388 reference stars in a cone of 20 arcmin centered on J1407 that are also observed by *SuperWASP*, R_{all}. The bottom panel in

[1] `http://keplergo.arc.nasa.gov/ContributedSoftwareKepcotrend.shtml`.

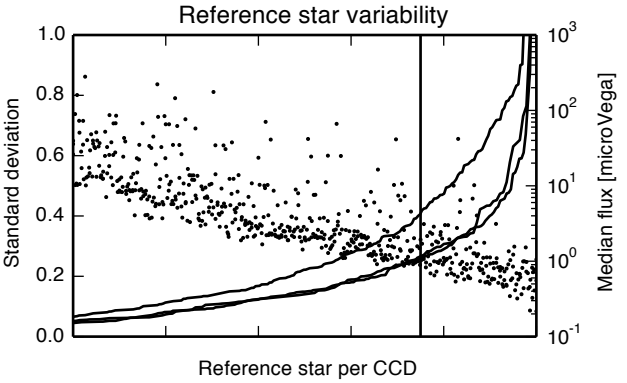

Figure 6.2: Flux variability (lines, left axis) and median flux (right axis, dots) for reference stars observed on the three different CCDs. The vertical line denotes the 75 per cent cut-off we chose for selecting quiet reference stars, only stars to the left are used in consequent de-correlation. While CCD 221 and 227 have similar variability roll-off, the upper solid line for CCD 228 indicates this CCD has noisier data. See text for details.

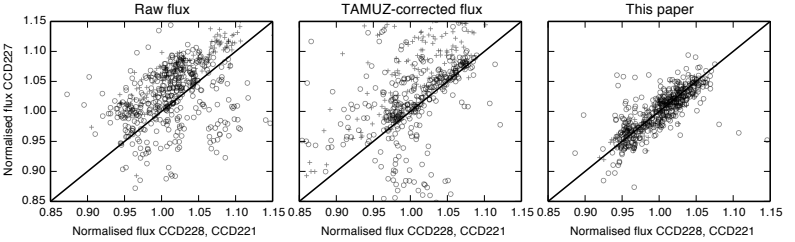

Figure 6.3: Hourly-binned flux from CCDs 221, 227 and 228 plotted against each other. The raw flux (FLUX) shows an offset between the CCDs as well as a significant scatter (Pearson's correlation coefficient $\rho = 0.49$), while the automatically reduced flux (TAMFLUX) is more consistent between different CCDs but still shows a large spread between the data ($\rho = 0.54$). The manually de-correlated flux shows no offset and significantly reduced scatter, indicating consistency between the three different CCDs ($\rho = 0.81$).

Fig. 6.1 shows the number of reference stars co-temporally observed with J1407, summed for all CCDs, averaged per day. Because of temporal gaps in both the target and reference data, we cannot perform a global analysis of a set of reference stars for our target star, and adapted the methods mentioned above to work on a point-by-point basis.

For each CCD separately, we used only reference stars for which at least 25 per cent of the data points are co-temporally observed with J1407, $\mathrm{R_{cotemp}}$.

$$\mathrm{R_{cotemp}} = \{x \in \mathrm{R_{all}} | \#(x_{\mathrm{exp}} \cup \mathrm{tgt_{exp}}) > 0.25\#(\mathrm{tgt})\}. \tag{6.1}$$

Of this subset we selected 75 per cent that have a low variance σ_{ref} (i.e. quiet stars), defined as the standard deviation of the median-normalised flux

$$\sigma_{\mathrm{ref}} = \mathrm{stddev}(F_{\mathrm{ref}})/\mathrm{median}(F_{\mathrm{ref}}). \tag{6.2}$$

We require photometrically quiet stars to measure the systematics of the cameras. This criterion was chosen to reject the most variable reference stars (see Fig. 6.2). In this way we obtained approximately 60 to 100 suitable reference stars, $\mathrm{R_{quiet}}$, per exposure of our target.

$$\begin{aligned}\mathrm{R_{quiet}} = \{x \in \mathrm{R_{cotemp}} | \\ \sigma(x/\mathrm{median}(x)) < \sigma(x/\mathrm{median}(x))_{75\%}\}.\end{aligned} \tag{6.3}$$

For this subset of reference stars, we calculated the mean of the median-normalised flux for all exposures co-temporal with our target.

$$F_{\mathrm{decorr}}(t) = \sum^{i \in \mathrm{R_{quiet}}} F_i(t)/\#(\mathrm{R_{quiet}}(t)) \quad \text{for } t \in t_{\mathrm{obs}}, \tag{6.4}$$

where t_{obs} are times at which J1407 was observed. We then divide the flux of J1407 by the thus obtained de-correlation vector F_{decorr} for each CCD.

Using the average of these reference stars suppresses any astronomical signal that might be present in an individual reference star, and any residual variation is then dominated by systematics. Since these stars are close to the target star, they are along nearly identical lines of sight through the atmosphere and camera optics, and so sample similar optical conditions. Additionally, these stars are close together on the CCD surface, such that they sample similar vignetting and electronic noise in the data.

Finally, to normalise the flux and allow inter-CCD comparison, we normalised the J1407 light curve by a first order polynomial fit for each CCD individually, excluding the transit window during MHJD 54 180 to 54 250.

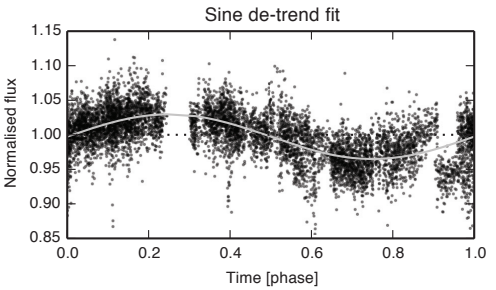

Figure 6.4: Normalised phase-folded *SuperWASP* flux for non-transit 2007 data with period 3.2011 ± 0.0002 d showing the stellar variability. The solid line is a best-fitting sinusoid with variable period.

Table 6.1: Measured period and period variability for J1407 in three years of *SuperWASP* data.

Season	Period [d]	Period change [s d^{-1}]	Amplitude [%]
2006	3.2183(4)	22(2)	4.98(3)
2007	3.2011(2)	31(1)	3.57(2)
2008	3.2066(3)	0.8(6)	5.00(2)

Through this de-correlation process, the photometry from the different CCDs now show significantly less scatter. The result is shown in Fig. 6.3, where the flux from different CCDs are plotted against each other.

Stellar variability de-trending

After successfully decorrelating the signal from the systematics, we then remove the stellar variability. Mamajek et al. (2012) find that the J1407 light curve shows a variability of approximately 3.21 d in the *SuperWASP* data, as expected from rotational modulation of star spots and a young star of ~ 16 Myr. Since this variability is independent of the transit signal, removing this signal is required for subsequent analysis.

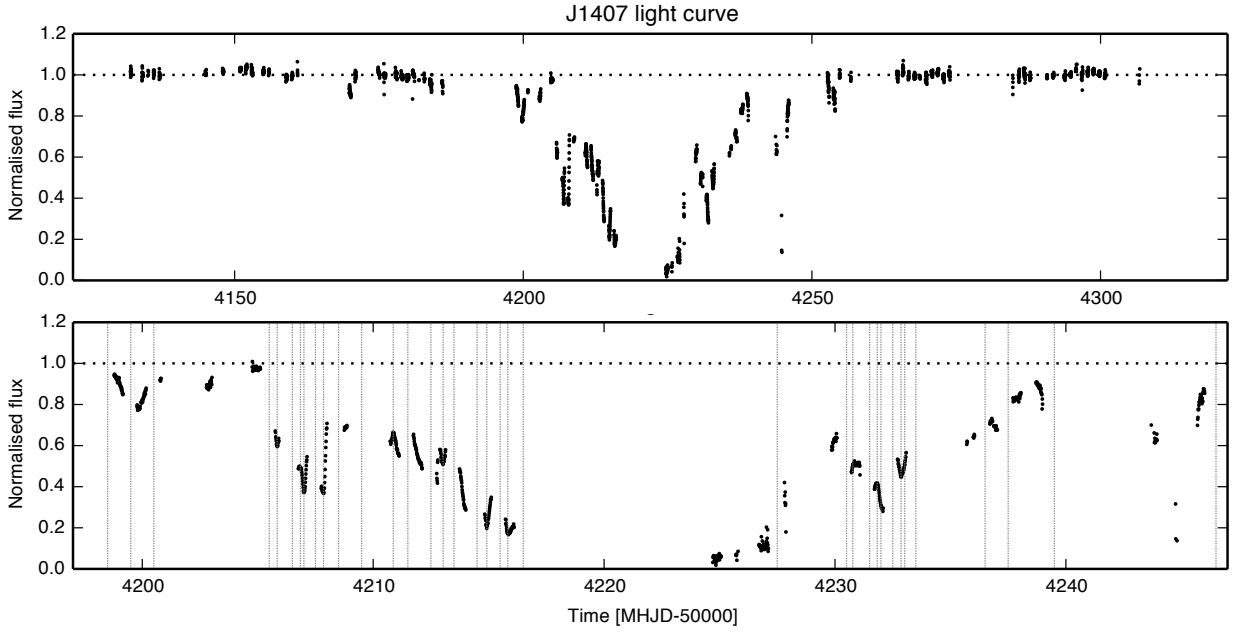

Figure 6.5: J1407 transit light curve as recorded by *SuperWASP* in 2007, corrected for systematics and stellar variability, binned in 15 min bins for clarity. Data are taken during the local night, daytime shows up as gaps. The eclipse midpoint is at approximately MHJD 54 222 and lasts at least 54 d with roughly symmetrical ingress and egress but asymmetry in the nightly variation. *Top:* overview of all of 2007. *Bottom:* zoom in on fine-structure during transit, with inflection points marked with vertical dotted lines.

First we investigate the stellar variability for each of the three seasons, 2006, 2007, and 2008. We use phase dispersion minimisation with a variable-period sinusoid as a model and use the Nelder-Mead fitting algorithm (Stellingwerf, 1978; Nelder & Mead, 1965). Our analysis shows that the best fitting periods and their amplitudes differ significantly from year to year (see Table 6.1). Furthermore, the amplitude of the variability is significantly less during the eclipse year 2007 than in the other years.

Initially we fit the variability for the 2006 and 2008 data with a constant period and interpolated this to the 2007 data. However, this interpolated fit mismatches the 2007 data in both phase and amplitude, it appears the period is not constant enough for such interpolation. To mitigate this, we fit the stellar variability using the light curve just before and after the transit in 2007, i.e. before MHJD 54 197 and after 54 255 where we verified by eye that little to no transit signal is present, by plotting the wrapped light curve and increasing the window size until a suitable window was found. Although additionally fitting the 2006 and 2008 data better constrains this variability, this requires modelling of stellar variability outside the scope of this paper.

For the out of transit 2007 data, we find a period of 3.2011 ± 0.0002 d. The phase folded light curve for this stellar variability period is shown in Fig. 6.4. Using the best fitting sinusoid we detrend the 2007 signal of interest as to remove the stellar variability.

The de-correlated and de-trended light curve for 2007 is depicted in Fig. 6.5, the top panel shows the whole year while the bottom panel shows 25 d around the approximate eclipse mid point MHJD 54 222 Ingress and egress show a similar trend of linearly decreasing opacity away from the eclipse mid point, but the nightly structure is very different from night to night.

6.3 Revised Stellar Parameters

Mamajek et al. (2012) presented estimated stellar parameters for J1407. Here we present updated stellar parameters based on slightly revised astrometry and assumed intrinsic stellar colors and temperature.

Using the revised proper motion for J1407 from the UCAC4 catalog (Zacharias et al., 2013, ; UCAC4 252-062736) and the space motion and convergent point solution for the Upper Centaurus-Lupus (UCL) subgroup from Chen et al. (2011), we estimate a revised (predicted) kinematic distance of 133 ± 12 pc ($\varpi = 7.49 \pm 0.65$ mas). This is consistent with the mean distance to the UCL subgroup from de Zeeuw et al. (1999): 140 pc.

Pecaut & Mamajek (2013) presented a revised sequence of intrinsic optical-infrared colors, effective temperature ($T_{\rm eff}$), and bolometric corrections as a function of spectral type for pre-main sequence (pre-MS) stars. Adopting the spectral type of K5±1 from Mamajek et al. (2012), and the intrinsic properties of K5 pre-MS stars from Pecaut & Mamajek (2013), we estimate slightly revised stellar parameters: $T_{\rm eff}$ = 4140^{+190}_{-120} K and $BC_J \simeq$ 1.58 ± 0.06 mag. Using the revised intrinsic colors for K5 pre-MS stars, and the $BVJHK_s$ photometry for J1407 compiled in Mamajek et al. (2012), we estimate that the star is statistically consistent with being unreddened, but adopt extinction A_J = 0.02 ± 0.02 (A_V = 0.06 ± 0.06 mag). Combining the revised extinction, parallax, and bolometric magnitude with the 2MASS J magnitude, we estimate the following parameters: $f_{\rm bol}$ = (6.09 ± 0.38) ~ 10^{-13} W m^{-2}, $m_{\rm bol}$ = 11.56 ± 0.07 mag, $M_{\rm bol}$ = 5.93 ± 0.20 mag, log(L/L$_\odot$) = -0.47 ± 0.08 dex. The slight change to the adopted $T_{\rm eff}$, and negligible change to the luminosity, shifts the stellar radius slightly: 1.13 ± 0.14 R$_\odot$. In Table 6.3, we summarize the inferred isochronal ages and masses using grids of pre-MS modern evolutionary tracks and isochrones. The median mass (~0.9 M$_\odot$) has changed negligibly, however the cooler $T_{\rm eff}$ has moved the star from the radiative track to the Hayashi track, and produced correspondingly younger isochronal ages (~10 ± 3 Myr). The isochronal ages of pre-MS K stars appear to be underestimated by nearly a factor of two compared to ages derived from the main-sequence turnoff, main-sequence turn-on, and Li depletion boundary ages (c.f. Pecaut et al., 2012; Bell et al., 2013; Soderblom et al., 2014). We continue to adopt the mean UCL age from Pecaut et al. (2012) (~16 Myr) as representative for J1407, but note that an age somewhere in the range of ~5–20 Myr is possible. We adopt a mass of 0.9 ± 0.1 M$_\odot$ based on the HR diagram position of J1407, noting that four of the five sets of pre-MS evolutionary tracks lead to inferred masses closely bracketing ~0.9 M$_\odot$. However, we note that if the inferred pre-MS isochronal ages may be in error by nearly a factor of ~2×, then the true masses may be systematically off by tens of percent as well (see e.g. Hillenbrand & White, 2004). At this point, we are not in a position to be able to quantify the magnitude of any potential systematic error in mass due to problems with the evolutionary tracks themselves.

In summary, the most significant change to the adopted parameters for J1407 is that the estimate radius is about 18 per cent larger compared to Mamajek et al. (2012). We adopt these new values as compiled in Table 6.2 in the following sections.

Table 6.2: Revised Stellar Parameters.

(1) Propery	(2) Value	(3) Ref.
α(J2000)	14:07:47.929	1
δ(J2000)	-39:45:42.75	1
μ_α	-24.3 $\pm$ 1.7 mas yr^{-1}	1
μ_δ	-19.4 $\pm$ 2.0 mas yr^{-1}	1
A_J	0.02 $\pm$ 0.02 mag	2
A_V	0.06 $\pm$ 0.06 mag	2
Dist	133 $\pm$ 12 pc	2
$T_{\rm eff}$	4140^{+190}_{-120} K	2
log(L/L$_\odot$)	-0.47 $\pm$ 0.08 dex	2
Age	$\sim$16 Myr	3
Mass	0.9 $\pm$ 0.1 M$_\odot$	2

References: (1) Zacharias et al. (2013), (2) this paper, (3) adopted UCL age from Pecaut et al. (2012), see discussion in text.

Table 6.3: Isochronal Age and Mass Estimates for J1407.

(1) Tracks ...	(2) Age Myr	(3) Mass M$_\odot$
Baraffe et al. (1998)	10	0.90
Siess et al. (2000)	12	0.88
Yi et al. (2003)	5	0.68
Dotter et al. (2008)	12	0.92
Paxton et al. (2011)[1]	9	0.87

[1] Evolutionary tracks and isochrones were generated using the MESA evolutionary code (Paxton et al., 2011), adopting the protosolar abundances from Asplund et al. (2009) (J. Strumpf, priv. comm.).

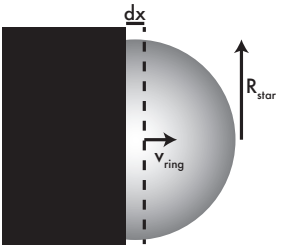

Figure 6.6: Eclipse geometry for an opaque ring crossing the star. In this scenario, no material is in front of the star before the ring arrives.

6.4 Ring model

After successfully removing instrument systematics and stellar variability, we investigate the fine structure in the light curve. Here we quantitatively investigate this to constrain the geometrical parameters of this system, by modelling the changes in intensity as being due to the passage of a ring edge across the disk of the central star. By measuring the gradient in the light curve and assuming a diameter for the star, we can derive a lower limit to the speed at which the occulting object is moving.

We model the eclipse geometry by assuming that an optically thick ring moves in front of the stellar disk. The stellar disk is approximated with a limb darkening model from Claret & Bloemen (2011b). We assume that the ring is circular and azimuthally symmetric around J1407b, that the diameter of the ring is much larger than the diameter of the star so that the edge of the ring can be approximated as a straight line, and that the edge of the ring is perpendicular to its direction of motion, as seen in Fig. 6.6. The observed light curve gradient dL/dt is given by the rate at which the surface of the star is eclipsed, multiplied with the mean intensity of the star in the eclipsed area. Below we calculate light curve gradients for a limb darkened star. These approximations then present a lower limit for the relative velocity of the ring system - if the ring edge is not perpendicular to the direction of motion, then the ring velocity will be higher for a given dL/dt. To explain the data, we require gradients in the light curve of up to $3\,L_\star\,d^{-1}$.

For our analysis, we use a linear limb darkening law from Claret & Bloemen (2011b):

$$I(\mu) = 1 - u(1-\mu), \tag{6.5}$$

with u is the limb darkening coefficient, $\mu = \cos(\gamma)$, where γ is the angle between the line of sight and the surface normal. For stars such as J1407

($T_{\rm eff} \sim 4500$ K, $\log g \sim 4.4$, [Fe/H] ~ 0), Claret & Bloemen (2011b) find limb darkening coefficient $u = 0.80 \pm 0.05$ in the *SuperWASP* band. We rewrite μ as linear coordinate $r = \sqrt{1-\mu^2}$ from 0 at the centre of the disk to 1 at the limb to yield:

$$I(r) = 1 - u(1 - \sqrt{1-r^2}). \tag{6.6}$$

The flux in a small vertical strip of width dx at the centre of the stellar disk is then given by

$$\begin{aligned} F_{\rm strip} &= dx \int_{-R}^{R} I(r/R)\, dr \\ &= dx\, 2\, R(1 - u + \frac{\pi u}{4}), \end{aligned} \tag{6.7}$$

while the total flux is given by

$$\begin{aligned} F_{\rm total} &= \int_0^R 2\,\pi r\, I(r/R)\, dr \\ &= \frac{1}{6} R^2\, \pi\, (6 - 2u), \end{aligned} \tag{6.8}$$

with R the stellar radius. The maximum light curve gradient is then given by the ratio of these, divided by the time dt it takes to cross distance dx, multiplied by the total stellar luminosity

$$\frac{dL}{dt}_{\rm max} = {\rm L}_\star \frac{F_{\rm strip}}{F_{\rm total}} \frac{1}{dt}. \tag{6.9}$$

We can rewrite this to obtain the implied speed for a given gradient as

$$\begin{aligned} \frac{dx}{dt}_{\rm min} &= \dot{L}\, R\, \pi \frac{2u - 6}{12 - 12u + 3\pi u} \\ &\approx 13\,{\rm km\,s^{-1}} \left(\frac{\dot{L}}{{\rm L}_\star\,{\rm d}^{-1}}\right)\left(\frac{R}{1.13\,{\rm R}_\odot}\right) \end{aligned} \tag{6.10}$$

where $v = dx/dt$ is the speed of the ring with respect to the star.

We now assume that J1407b is in a circular Kepler orbit around the central star with velocity v and semi-major axis a:

$$\begin{aligned} a &= G\, M / v^2 \\ &\approx 8.0\,{\rm AU} \left(\frac{M}{0.9\,{\rm M}_\odot}\right)\left(\frac{v}{10\,{\rm km\,s^{-1}}}\right)^{-2}, \end{aligned} \tag{6.11}$$

and a disk diameter of

$$\begin{aligned} r_d &= v\, t_{\rm eclipse}/2 \\ &\approx 0.16\,{\rm AU}\left(\frac{t_{\rm eclipse}}{54\,{\rm d}}\right)\left(\frac{v}{10\,{\rm km\,s^{-1}}}\right). \end{aligned} \tag{6.12}$$

Equation (6.12) is equivalent to Eqn. 10 in Mamajek et al. (2012), although the authors missed a factor π in their equation. We can express the radius of the disk as a fraction of the Hill radius $r_{\rm H} \equiv a(\mu/3)^{1/3}$, with $\mu = m_2/(m_1 + m_2)$ as

$$\begin{aligned} \frac{r_d}{r_{\rm H}} \equiv \xi &= t_{\rm eclipse}\, v\, \frac{3^{1/3}}{a\,\mu^{1/3}} \\ &= 0.28\left(\frac{t_{\rm eclipse}}{54\,{\rm d}}\right)\left(\frac{v}{10\,{\rm km\,s^{-1}}}\right)^3\left(\frac{M}{0.9\,{\rm M}_\odot}\right)^{-2/3}\left(\frac{m_2}{{\rm M_J}}\right)^{-1/3}. \end{aligned} \tag{6.13}$$

To measure the light curve gradient for J1407, we fit straight lines to manually selected windows with constant gradient. An overview of the light curve is shown in Fig. 6.7, where straight line fits are plotted over the data. The top panel shows the light curve during the transit and each panel below shows one night of data. We plot the measured light curve gradients in Fig. 6.8.

6.5 Results

A wealth of fine structure becomes visible in the light curve (Fig. 6.5 and Fig. 6.7). By decorrelating against reference stars we ensure these are not randomly occurring systematic effects, but are due to J1407. Removing the stellar variability further improves the photometry.

The light curve shows strong gradients of up to 3 $L_\star\ d^{-1}$, which means that the eclipsing agent has a speed to occult the star in roughly 1/3 of a day. Furthermore, we find a myriad of fine structures in the light curve, with at least 24 inflection points on ingress, and 16 on egress (see Table 6.4 and Fig. 6.7), and changes of at 15 per cent or more in flux in 6 nights. Some inflection points are directly observed in the nightly data, whilst others are implied by a mismatch in photometric observations between consecutive observation windows, implying an unseen change in light curve gradient. These inflection points indicate the presence of at least 24 different rings in the J1407b system. This ring structure is tentative indication of the presence of shepherding moons, without which the ring structure would be smeared out radially on short dynamical timescales.

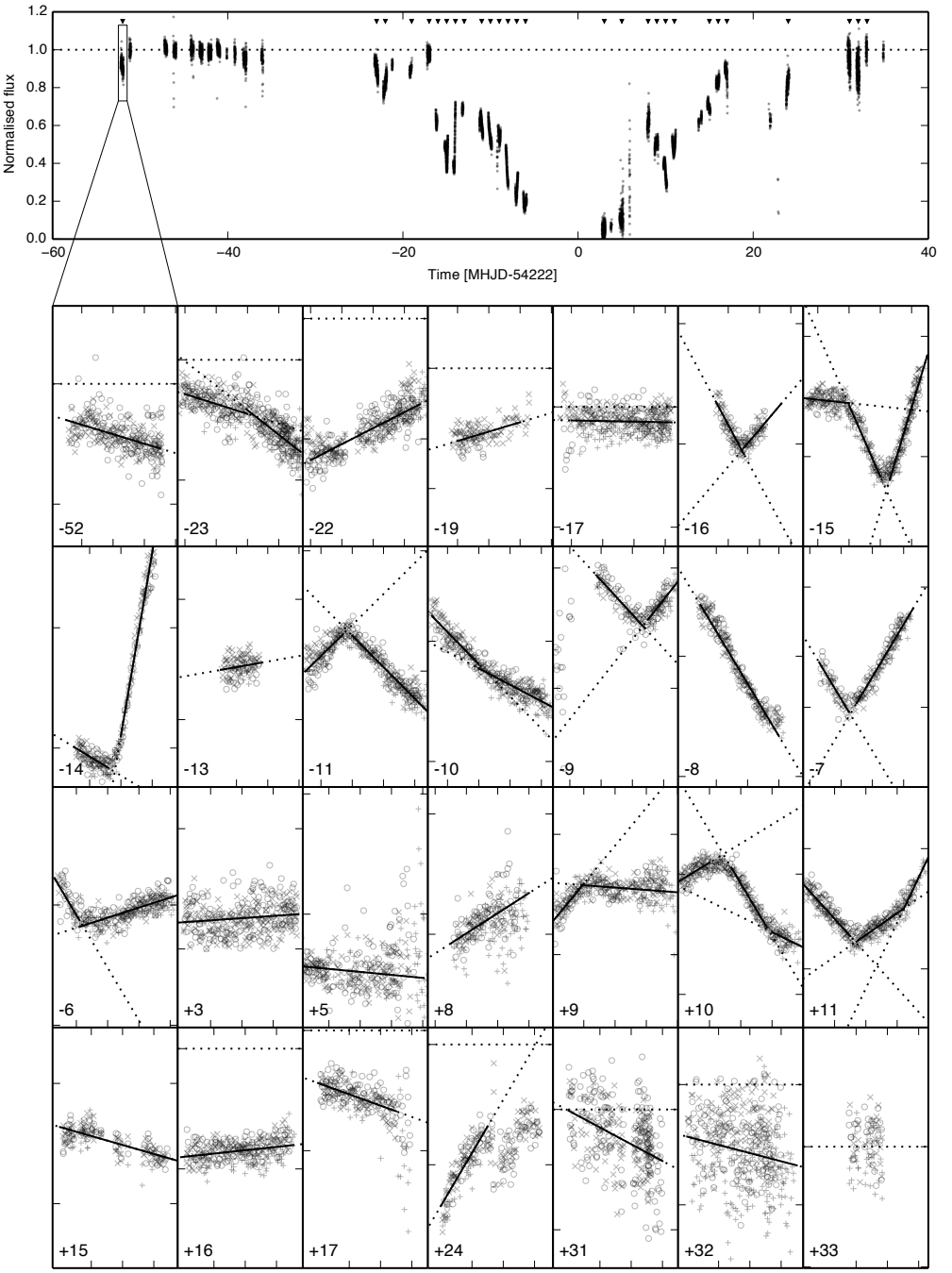

Figure 6.7: Detailed plot of the J1407 light curve during the transit. *Top*: overview of the light curve. *Bottom*: nightly light curve for 28 nights during the transit, indicated in the upper panel by triangles. The straight line fits are plotted over the data, a solid line is the window used for the fit, a dotted line is extrapolated. The y-ticks are spaced at 0.2 AU (as in the top panel) and x-ticks at 0.1 d.

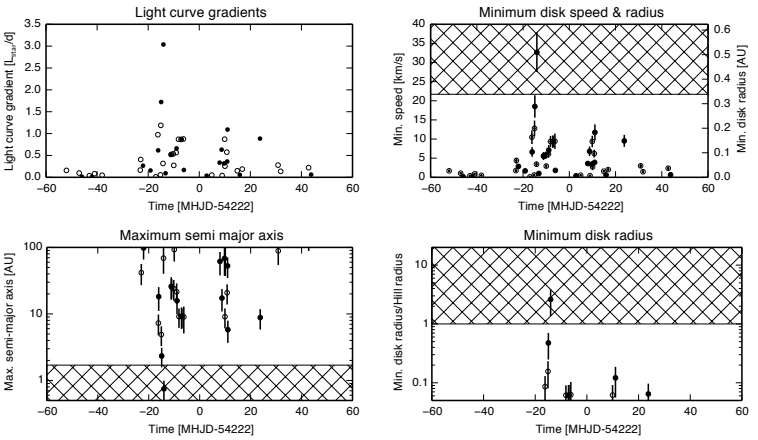

Figure 6.8: Light curve gradients and derived system parameters for circular orbits. *Top-left*: light curve gradients during the transit, *top-right*: disk speeds and radii, *bottom-left*: semi major axes, *bottom-right*: disk radius over Hill radius, assuming $m_2 = 50\,M_J$. The transit mid point is approximately at MHJD 54 222. Filled circles are positive gradients (i.e. increasing flux), open circles represent negative gradients. The hatched area represents data incompatible with the minimum period of 2.3 yr (lower-left and top-right) or data that predict disks larger than the Hill radius (lower-right).

Given the light curve gradients we measure and an estimate of the diameter of the star, we can compute the physical speed and diameter of the ring system. Using $R = 1.13 \pm 0.14\,R_\odot$, $M = 0.9 \pm 0.1\,M_\odot$, $t_{\rm eclipse} = 54$ d (Mamajek et al., 2012), and $u = 0.80 \pm 0.05$ (Claret & Bloemen, 2011b) gives the results shown in Fig. 6.8. The error bars are dominated by the 16 per cent error in the radius, an improved estimate for this would better constrain the disk parameters.

Most nights have $<15\,\mathrm{km\,s^{-1}}$ occultation speeds, but two nights during ingress have exceptionally high speeds. These gradients are 1.7 and 3.0 $L_\star\,d^{-1}$, which correspond to 22 ± 3 to $38 \pm 5\,\mathrm{km\,s^{-1}}$, respectively. While the first night is compatible with the $21.7\,\mathrm{km\,s^{-1}}$ upper limit found by Mamajek et al. (2012), the second night is not. Additionally, the highest speeds combined with the 54 d transit time yield a disk radius of 0.3 AU and 0.6 AU, respectively.

Furthermore, we observe significant change in gradients on the timescale of hours in the data, for example during nights –16, –15, –14, –11, 10 and 11 in Fig. 6.7, showing inflection points where the gradient changes. This ratio of the variability timescale of an hour over half the transit duration of

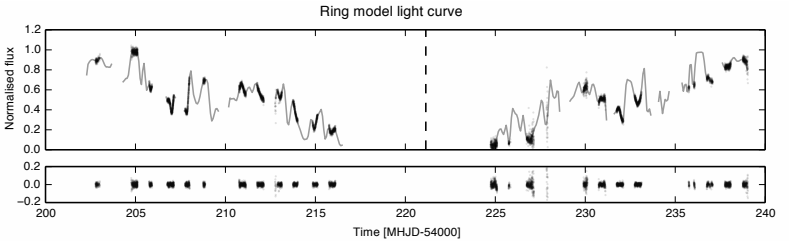

Figure 6.9: Example ring system model light curve corresponding to the geometry shown in Fig. 6.10. The top panel shows the data (black dots) with the model (solid line), the bottom panel shows the residuals of this fit. With 150 rings, the light curve variability can be accounted for, including the steep gradients in some nights. The dashed vertical line indicates the center of the ring system.

54 d implies an aspect ratio of the disk of $h/r \approx 0.0015$, confirming earlier findings by Mamajek et al. (2012).

6.6 Initial ring fitting

After removing instrument systematics and de-trending the signal from stellar variability, we fit a toy ring model to the light curve. The ring system is modeled as a infinitely thin, filled disk with radius $R_{\rm disk}$ consisting of N, equal-width rings each with linear transmission T between 0 and 1. This ring system is rotated under inclination i and azimuth ϕ to match the unknown geometry of the target system. The center of the ring system is located at t_0, the star with diameter d_s impacts at b. The stellar diameter and impact parameter are expressed in days to match the observational data. A best-fitting ring model (detailed below) is shown in Fig. 6.10.

From this ring model we crop out a horizontal section across the full width of the system with the height of the stellar diameter d_s, which in these units is on the order of 0.2 d (see Fig. 6.10). We digitize this section of the model at a resolution of 50 pix d^{-1} and set the pixel values to the transmission T of the ring at that position. We then compute the simulated light curve by convolving the horizontal section with a stellar profile with unit integrated intensity.

A model with fixed radius and number of rings is then fit to the data, using a Nelder-Mead algorithm for all parameters except the ring opacities which are fit using least squares minimisation. The fitting is nested this way because the ring transmissions have a clear optimum value, as opposed to the system orientation. Using least-squares fit where possible

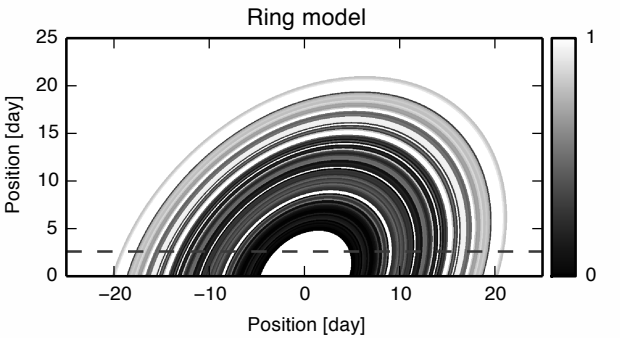

Figure 6.10: Example ring system with 150 rings of variable transmission (indicated by grayscale) extending up to 25 d out on either side of the eclipse mid point rotated under inclination $i = 0.83$ rad and azimuth $\phi = 2.4$ rad with stellar impact parameter $b = 2.6$ d. The stellar path across the ring system is indicated by the dashed horizontal line. Note that this model is one possible fit, but is by no means unique. The associated light curve is shown in Fig. 6.9.

speeds up the fitting significantly, allowing more rings to be fit in the same time.

We find that using 150 rings for the 25 days around the eclipse mid point gives a satisfactory of the light curve up to the hourly variability, as shown in Fig. 6.10. This best-fitting model is by no means unique, this is only one possible ring model. The sparsity of the data makes ring matching between ingress and egress difficult. Nonetheless, this fit indicates that a ring model is compatible with the data. Future work should include model constraints imposed by resonant gaps introduced by moons as well as a more thorough analysis of the parameter space.

6.7 Discussion

The minimum speeds derived only from the light curve gradients, stellar radius and limb darkening are incompatible with both the minimum period of 2.3 yr found by Mamajek et al. (2012), in spite of the large uncertainties on stellar properties. Also using the stellar mass and a secondary mass upper limit of 50 M_J (Kenworthy, priv. comm.), the disk is also overfilling the Hill radius for the largest minimum speed. Here we briefly consider two scenarios that could mitigate these problems, the first being an elliptical orbit and the second substructure in the rings.

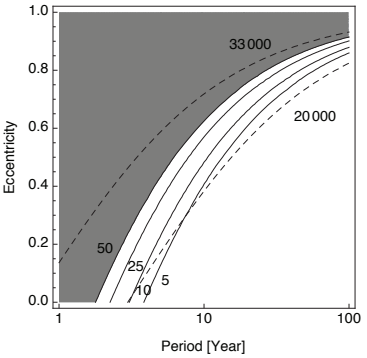

Figure 6.11: Secondary mass for $R_{\rm disk} = R_{\rm Hill}$ in M_J (solid lines) and maximum orbital speed in m s^{-1} (dashed lines), both as function of period and eccentricity. For a given secondary mass (solid line), the area below the line is allowed: in those cases the eccentricity is less, giving a larger minimum separation and thus a larger Hill radius, thus fitting in the disk. For a given speed (dashed line), the area above the curve is allowed: in those cases the eccentricity is higher and thus the maximum speed is larger. For the highest speed calculated from the light curve gradients there is no region compatible with stable rings given that the secondary mass is limited to 50 M_J. The second highest speed could be explained by ellipticity with a <3 yr orbit, or with a secondary mass of 25 M_J above that.

Ellipsoidal orbits for J1407b

An ellipsoidal orbit would allow for larger periastron speeds and explain the anomalous velocities implied in the data, however these are not fast enough to explain the observations. For a Kepler orbit with period P and ellipticity e, we compute the maximum speed at periastron

$$v_{\rm max} = \left(\frac{2\pi\, G\, M}{P}\right)^{1/3} \left(\frac{1+e}{1-e}\right)^{1/2}. \tag{6.14}$$

These speeds are plotted as dashed lines in Fig. 6.11. This maximum speed combined with the transit duration of 54 d gives a disk radius. Additionally, for a planetary mass m_2 we can compute the Hill radius at the periastron

$$R_{\rm Hill} = \left(\frac{m_2\, G\, P^2}{12\pi^2}\right)^{1/3} (1-e). \tag{6.15}$$

We then solve $R_{\rm disk} = R_{\rm Hill}$ using Eqs. (6.12)–(6.15) for m_2, plotted as solid lines in Fig. 6.11. Since the secondary mass is less than 50 M_J (Kenworthy, priv. comm.), ellipticity alone cannot explain the speeds derived from the observed gradients.

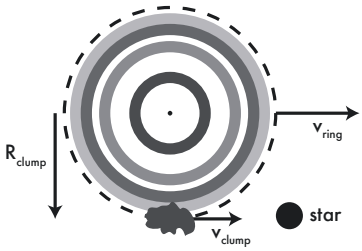

Figure 6.12: Geometry of a clump in a circular orbit around J1407b eclipsing the star. In this case, the speed of the disk with respect to the star ($v_{\rm ring}$) vectorially adds to the speed of the clump in the ring ($v_{\rm clump}$). Outer rings are not shown for clarity.

Azimuthal structure in the rings

If there is non-radial structure in the ring, e.g. a bar or clumps in the ring, this could give rise to an increased gradient dL/dt. Such radial structures ('spokes') have been observed in the B-rings of Saturn (Smith et al., 1982). With azimuthal density structures in the ring, these could vectorially add to the observed light curve gradient, as shown in Fig. 6.12. The night showing the highest light curve gradient is at approximately 14 days before the eclipse mid point. Assuming $m_2 = 50\,{\rm M_J}$ and $P = 3.5\,{\rm yr}$ (Kenworthy, priv. comm.), this would give an orbital speed of the planet of $v_{\rm ring} = 19\,{\rm km\,s^{-1}}$ such that the ring distance would be at $19\,{\rm km\,s^{-1}} \times 14\,{\rm d} = 0.15\,{\rm AU}$. For this radius, the ring would rotate at a speed of $v_{\rm clump} = 17\,{\rm km\,s^{-1}}$ which in total would yield a occulting speed of $36\,{\rm km\,s^{-1}}$, compatible with the observations.

Forward scattering

A third option is that the observed gradient is a combination of the gradient from a ring eclipsing edge added with an additional gradient due to forward scattering from the particles making up the ring wall. Such forward scattering is seen and modelled in Fomalhaut's debris disk (Kalas et al., 2005) and in the light curve produced by a disintegrating exoplanet KIC 12557548 b (Rappaport et al., 2012; Brogi et al., 2012). Since we do not know the thickness of the disk and a unique ring geometry, we do not carry out the modeling in this paper.

6.8 Conclusions

We have reduced the *SuperWASP* extracted photometric flux data for J1407 using an ensemble of photometrically quiet nearby reference stars to remove systematic effect in the data, and detrended for stellar variability, showing an improvement over the raw flux as well as the automatically reduced flux pipeline outputs. We find a periodicity of approximately 3.2 d for the different observation seasons, with significant differences between the seasons. We attribute the difference in observed rotational periods due to the change in the mean latitudinal position of star spots on the surface of J1407 and the differential rotation of the stellar atmosphere.

With the new photometry, we have investigated the nightly structure in the light curve during transit and find strong gradients of up to $\sim$3 $L_\star$ per day. Furthermore, we find a myriad of fine structures in the light curve, which we explain with the transit of a ring system orbiting around J1407b and we identify at least 24 different rings. Given that for a disk alone this structure would be radially smeared out by internal disk interactions on short dynamical timescales, this is indicative of the presence of shepherding exomoons.

We constructed a toy ring model to fit the light curve data and find a good fit can be obtained using 150 rings when using the inner 25 d of light curve around the eclipse mid point. Although we stress that this solution is by no means unique, it does indicate that a ring model can be compatible with the data. An improved model is required as well as a more thorough search through the parameter space for better understanding of the system.

Using a simple model of a limb-darkened star, we calculate the minimum transit speed implied by the observed light curve gradients. We find that these minimum speeds are incompatible with the analysis by Mamajek et al. (2012) who find a minimum period of 2.3 yr. Although an elliptic orbit could alleviate this problem to some extent, it cannot completely explain the largest gradients in the light curve. We propose sub-structure in the rings in forms of clumps (appearing as "spokes") as a plausible explanation for the observed gradients.

Further observations to constrain the orbital period and mass of J1407 are required to better understand this system. ALMA is capable of directly detecting rings down to 0.8 M_{moon} masses (as estimated by Mamajek et al. (2012)) in a few hours, and its spatial resolution would enable a unique confirmation of the bound orbit of J1407b around J1407. Several small telescopes are currently monitoring for the beginning of the next eclipse, and an intensive monitoring campaign to cover the duration of the 60 d eclipse

Table 6.4: Inflection points in the J1407 light curve gradient indicative of opacity change. Each inflection point indicates a change in gradient, which in turn implies change in opacity, and thus a new ring beginning to transit the star. Time is shown in MHJD−54 222. The numbers marked with an asterisk are approximate, indicating the presence of an inflexion point during daylight hours but whose presence is implied by the light curves in adjacent photometric measurements. See also Fig. 6.7.

Inflection point [d]				
Ingress			Egress	
−52.5*	−15.15	−9.5*	5.5*	11.02
−51.5*	−15	−8.97	8.5*	11.5*
−23.5*	−14.5*	−8.5*	8.77	14.5*
−22.5*	−14.15	−7.5*	9.5*	15.5*
−21.5*	−13.5*	−7.08	9.83	17.5*
−16.5*	−12.5*	−6.5*	9.99	24.5*
−16.155	−11.13	−6.17	10.5*	31.5*
−15.5*	−10.5*	−5.5*	10.86	32.5*

would give an unprecedented opportunity for the resolved study of a protoplanetary ring system outside our Solar system. Spectroscopy over a broad range of wavelengths can characterise the density and composition of the rings, providing new insight into their formation and origins. The high rotational of the star, combined with high resolution spectroscopy, leads to the exciting possibility of observing the Rossiter-McLaughlin effect (Rossiter, 1924; McLaughlin, 1924) as the ring edges transit the stellar disk and a subsequent increase in spatial resolution in the ring structure. Initial modelling efforts by our group show that a continuous time coverage using multiple telescopes spread over different latitudes will be essential in constraining the system and determining the ring geometry present there.

Acknowledgments

The WASP project is funded and operated by Queen's University Belfast, the Universities of Keele, St. Andrews and Leicester, the Open University, the Isaac Newton Group, the Instituto de Astrofísica de Canarias, the South African Astronomical Observatory and by STFC.

Table 6.5: Measured light curve gradients greater than 0.1 d^{-1} and derived circular orbital speed. Time is shown in MHJD−54 222.

Time [d]	Gradient [d^{-1}]	Speed [km s^{-1}]	Time [d]	Gradient [d^{-1}]	Speed [km s^{-1}]
−52.00	−0.16(2)	−2.0(3)	−7.12	−0.86(7)	−11(2)
−23.10	−0.16(2)	−2.1(4)	−6.96	0.87(2)	11(1)
−22.92	−0.41(3)	−5.2(7)	−6.23	−0.9(1)	−11(2)
−22.02	0.270(9)	3.4(4)	−6.04	0.17(1)	2.1(3)
−19.10	0.16(3)	2.0(4)	7.97	0.33(4)	4.2(7)
−16.19	−0.97(6)	−12(2)	8.75	0.63(6)	8(1)
−16.09	0.62(7)	8(1)	9.75	0.32(5)	4.0(8)
−15.05	−1.19(4)	−15(2)	9.93	−0.87(3)	−11(1)
−14.91	1.72(4)	22(3)	10.05	−0.26(7)	−3(1)
−14.19	−0.32(4)	−4.0(7)	10.77	−0.58(3)	−7(1)
−14.04	3.04(6)	38(5)	10.94	0.36(2)	4.6(6)
−11.19	0.52(5)	7(1)	11.06	1.09(9)	14(2)
−10.97	−0.52(1)	−6.6(8)	14.90	−0.15(1)	−1.9(3)
−10.18	−0.54(3)	−6.8(9)	16.82	−0.19(2)	−2.4(4)
−9.98	−0.27(1)	−3.5(5)	23.77	0.88(5)	11(2)
−9.04	−0.57(3)	−7(1)	30.85	−0.28(3)	−3.5(6)
−8.90	0.66(6)	8(1)	31.88	−0.14(3)	−1.7(4)
−8.12	−0.87(2)	−11(1)	42.80	−0.22(2)	−2.8(4)